Small Molecule Inhibitors of Complex IV Induce Imbalanced Pyrimidine Expansion in OXA1L Variant Cells

Thomas W. Hanigan*, Junichiro Takaya, Haoxin Li, Jarret R. Remsberg, Verena Albert, J.C. Ducom, Christopher M. Joslyn, Scott C Henderson, Kathryn S Spencer, Sabrina Barbas, Melissa A Dix, Kim Masuda, Enrique Saez, Kenji Sasaki, Christopher G. Parker, Benjamin F. Cravatt*

Department of Molecular Medicine, The Scripps Research Institute, La Jolla, CA, USA.

*To whom correspondence should be addressed; Email: thanigan@scripps.edu, cravatt@scripps.edu

Abstract

Strategies to selectively target the altered mitochondrial metabolism of cancer cells are limited. Here we disclose small molecules identified from a library of fully functionalized probes (photoreactive, clickable) that inhibit the electron transport chain at complex IV (CIV), leading to a proliferative defect in a subset of cells harboring a repeat expansion in the CIV insertase OXA1L. Through photolabeling studies, we demonstrate preferential engagement of wild type OXA1L and show that resistance is frequently acquired through amplification or *de novo* mutation of OXA1L or its substrate MT-CO1. We find that the variant isoform decreases substrate affinity and post-transcriptionally stabilizes CIV independent of complex I, promoting dihydroorotate dehydrogenase (DHODH) coupled respiration. In heterozygous cells, glutamine maintains DHODH coupled respiration in the presence of inhibitor, leading to imbalanced pyrimidine expansion, nuclear DNA damage and mitotic cell death despite compensatory glycolytic flux. In contrast, anaerobic glycolysis and pyrimidine salvage sustain proliferation in the absence of oxygen reduction in homozygous cells. Consistent with this mechanism we find inhibition of DHODH antagonizes growth arrest induced though CIV and cells with basal or acquired resistance through OXA1L amplification are sensitive to pyrimidine antimetabolites. Our results identify small molecules to selectively target a novel druggable vulnerability, and context to identify and modulate sensitivity to a commonly used chemotherapeutic.

Main

Transformation and unchecked proliferation are driven by rerouting metabolic intermediates for biosynthesis and redox demands. In general, cancer cells increase glucose uptake, but reduce pyruvate to lactate in the presence of oxygen[1], which regenerates nicotinamide adenine dinucleotide (NAD) for sustained glycolytic ATP production. However, functional mitochondria are still required to support proliferation in a subset of cancers[2-6]. As an alternative to pyruvate, cancer cells frequently utilize glutamine for anaplerosis (glutaminolysis), and oncogenic transformation by KRAS and c-MYC, result in glutamine dependence[7]. Although glutamine can sustain anabolism, its metabolism produces ammonia in the mitochondrial matrix and disrupts the primary connection between mitochondrial respiration and glycolysis. Thus, the ability of cells respiring on glutamine to adapt cellular metabolism to altered substrate availability or drug perturbation may be limited and could provide a therapeutic window beyond increased proliferation rate.

Results

Small Molecules Targeting a Subset of Complex IV Dependent Oxygen Consumption Selectively Inhibit Proliferation

Towards this goal, we screened a library 292 small molecules functionalized with a photoreactive group and biorthogonal handle[8] in two genetically defined NSCLC lines with differential basal proliferation rate using an end-point viability assay, and counter screened hits by measuring growth rate inhibition metrics from cell count over a prolonged period in five additional GFP-labeled cell lines (**Figure 1c,d, Supplementary Table S1**). In this fashion, we identified three compounds (hit rate of 0.00958) that inhibited viability with greater than 3-fold selectivity ($P<0.002$, **Supplementary Figure 1a-c**), one of which (BMT-819) remained selective independent of growth rate, and decreased cell count without significantly inhibiting proliferation in two of the additional five cell lines (**Figure 1d**, **Supplementary Table S1**)[9].

Based on the two ringed quinoline/tetrahydroquinoline scaffold of BMT-819, we synthesized a library of structural analogues lacking the fully functional handle (**Figure 1b**) and identified two compounds with improved potency (**Supplementary Figure 1c**). Both analogues retained a two-ring aromatic system, either a naphthalene or 2-methoxy methyl quinoline ring, optimally connected at the 4- position to an N-alkyl tetrahydroquinoline via an ethoxy ethyl linkage (**Figure 1b**). Using the most potent analogue (B508, **Figure 1b**), we evaluated viability and proliferation in an additional 37 cell lines from lung, breast, prostate, and colorectal lineages (**Figure 1e**, **Supplementary Table S1**). To negate differences in potency observed across basal medium types (**Supplementary Table S1**), we used a standardized formulation based on minimum essential medium supplemented with glucose, non-essential amino acids (including aspartate and glutamine) and pyruvate. In addition to B508, we screened the non-selective anti-mitotic paclitaxel, as well as pyrimidine antimetabolite 5-Fluorouracil (5-FU) (**Figure 1e, Supplementary Table S1**)[9-11]. This analysis demonstrated that B508 inhibited the viability of a subset of eight cell lines without significantly affecting an additional 22 (Difference in IC_{50} > 350-fold). Remarkably, B508 potency was inversely correlated with sensitivity to 5-FU (r^2 = 0.842, **Figure 1e**), which significantly inhibited viability in eight cell lines.

To ascertain underlying biological determinants driving sensitivity, we conducted an integrated analysis of genome, transcriptome, and proteome across cell lines cultured under the same conditions used for viability screening (**Supplementary Table S1**, **Supplemental Table S3**). This analysis revealed that in addition to being predominantly KRAS/LKB1 mutant and mismatch deficient, sensitive cells had a significant upregulation of nuclear encoded proteins of the mitochondrial ribosome as well as rate-limiting mitochondrial constituents of the urea cycle and pyrimidine biosynthesis (**Supplementary Figure 2d**, **Supplementary Tables S3**). Notably, while mitochondrial proteins were positively correlated with compound sensitivity, transcript abundance was inversely related (Pearson r = 0.77, P Value = 0.0124**,** **Supplemental Table S3**); indicative of a post-transcriptional stabilization. Consequently, we measured mitochondrial function via respirometry in response to B508 or inactive analogue 143-01 across our cell line panel in uniform medium (**Figure1f-k**, **Supplementary Figure 1f-h**)[12]. Acute treatment with B508, but not inactive analogue 143-01, dose-dependently inhibited oxygen consumption, which was retained after uncoupling with FCCP, consistent with inhibition of complex IV (**Figure 1f**).

To determine the effects of B508 on the activity of individual OxPhos complexes I, II, III and IV we conducted a biochemical analysis of NADH oxidation, 2,6-dichlorophenolindophenol (DCPIP) reduction, or cytochrome c reduction and oxidation respectively, in comparison to known OxPhos inhibitors in enriched mitochondria[13]. Consistent with the respirometry, we found B508 dose dependently inhibited the rate of oxidation of exogenous cytochrome c through complex IV (IC_{50} = 0.055 μM), like the irreversible inhibitor KCN, while increasing the rate of decylubiquinol reduction through complex III by 1.5-fold that of basal levels, which was eliminated by treatment with complex III inhibitor Antimycin A (**Figure 1k**). In addition to complex IV, we found B508 reduced the rate of NADH oxidation through Complex I in comparison to rotenone, without significantly decreasing DCPIP reduction through complex II in the presence of succinate and exogenous ubiquinone, which was sensitive to excess complex II inhibitor malonate (**Figure 1k**). Whereas B508 dose-dependently inhibited cytochrome c oxidation in mitochondrial extracts, we did not observe a measurable change in whole cell lysates prepared from cells expressing the cytoplasmic ubiquinone reductase NQO1 or control, provided exogenous quinone (**Supplemental Figure 2b**), and we found the relative potency of cytochrome c oxidase inhibition in enriched mitochondria was 3.2-fold less than in living cells, suggesting that B508 activity requires an

intact mitochondrial membrane potential (ΔΨm). In support of this conclusion, TMRM loading in the nonquenching mode followed by acute treatment with B508, in addition to CMTMRos staining after 3-hour exposure demonstrated that ΔΨm was increased in sensitive cell lines despite reduced OCR (**Supplementary Figure 2f**, **Figure 4g**). Taken together these experiments suggest that BMT-819/B508 inhibits mitochondrial cytochrome c oxidase activity but a subset of oxidative phosphorylation is maintained through ubiquinol reoxidation at complex III in the presence exogenous substrate.

As opposed to general cytotoxicity, inhibition of complex IV was accompanied by an immediate dose-dependent increase in extracellular acidification (ECAR) across cell lines (**Figure 1g**)[14]. The B508 induced ECAR was decreased by 2-deoxyglucose (**Supplementary Figure 2a**), and analysis of central carbon metabolites via mass spectrometry showed a significant increase in the relative fraction of ^{13}Carbon glucose labeled lactate and total lactate abundance (**Supplementary Figure 1e**, **Figure 2c**), indicative of increased glycolytic flux. As extracellular acidification promotes reliance on oxidative metabolism[15,16], we measured proliferation via cell count with regular medium exchange (**Figure 1j**). Despite maintenance of ATP, and the ratio of ATP/ADP (**Supplemental Figure 2e**), cell count was decreased after three to five doublings in sensitive cells, suggesting acidification or energy crisis does not underlie proliferative defect (**Figure 1j**). In contrast, proliferation was maintained indefinitely across resistant cells, provided regular supply of glucose containing medium, which was lost upon substitution of galactose for glucose, establishing that glycolysis is sufficient to maintain proliferation in this context (**Figure 1j**). As opposed to inhibitors of complex I[17], basal levels of mitochondrial oxygen consumption after removal of non-mitochondrial OCR and normalization to cell count[12,18], was not significantly correlated with sensitivity to BMT-819/B508, and the EC_{50} for inhibition was relatively invariant in comparison to viability (**Figure 1h**, **Supplementary Figure 1g**). However, the magnitude decrease in mitochondrial OCR in the presence of saturating concentrations of B508 (**Figure 1h**, **Supplementary Figure 1g**) plateaued at an average of 47% of control in comparison to 32% across ten sensitive versus resistant cell lines (**Figure 1h,** P Value < 1e-10), despite comparable increase in glycolytic flux (**Figure 1i, Supplementary Figure 1g**). In addition to glucose, glutamine can fuel oxidative metabolism[19]. Consistently, supplementation with glutamine selectively stimulated OCR across sensitive cells and the residual respiration retained in the presence of B508, was lost upon removal of glutamine from the medium (**Supplemental Figure 2a**)[20]. Moreover, sensitive as opposed to resistant cell lines required glutamine for basal proliferation (**Supplemental Figure 2a**). These experiments suggest that glutamine maintains basal proliferation and a subset of oxidative metabolism in the presence of inhibitor across sensitive cell lines.

DHODH Dependent Oxygen Consumption is Maintained in the Presence of Inhibitor Leading to Imbalanced Nucleotide Pools and Mitotic Catastrophe

In addition to complexes I and II, *de novo* pyrimidine biosynthesis through dihydroorotate dehydrogenase (DHODH) transfers electrons through ubiquinone to complex III in the inner mitochondrial membrane (**Figure 2b**)[21], and depends on glutamine derived nitrogen for synthesis of its substrate[22]. To determine whether DHODH activity was associated with B508 induced ubiquinol oxidation, we developed a targeted LC/MS based assay following the incorporation of ^{15}N-glutamine into 210 nitrogen containing pyrimidine metabolites across cell lines in log-phase growth. In line with the basal upregulation of mitochondrial components of *de novo* pyrimidine biosynthesis (**Supplemental Figure 2d, Supplementary Table S3**), the relative isotopologue abundance of glutamine labeled orotate (M+1) at steady state was two-fold higher in sensitive cells (**Figure 2a, Supplementary Figure 3d**).

Consistent with biochemical assays showing increased complex III activity, we found B508 treatment led to a 2-fold expansion of M+1 labeled orotate relative to the total pool, which was prevented by inhibition of DHODH (**Figure 2a**). Despite feedback inhibition of *de novo* pyrimidine biosynthesis at CAD (carbamoyl-phosphate synthase 2, aspartate transcarbamylase, dihydroorotase complex) by pyrimidine end-product uridine-5'-triphosphate (UTP)[23], the increased DHODH activity associated with B508 treatment occurred in the presence of exogeneous uridine and lead to a selective expansion in total abundance of pyrimidine triphosphates without depleting the essential precursor carbamoyl-phosphate across sensitive cell lines (**Figure 2c**). Importantly, pyrimidine expansion occurred without a concomitant increase in purine abundance (**Supplemental Figure 3a,c**), leading to an imbalance in the pyrimidine to purine nucleotide ratio conducive of genomic instability[24]. Contrastingly, uridine supplementation led to a decrease in the relative abundance of M+1 labeled orotate and B508 treatment selectively increased the incorporation of 2-^{13}C-1,3-$^{15}N_2$-uridine into M+3 labeled pyrimidine nucleotide triphosphates relative to the total pool across resistant cell lines (**Figure 2a-d**). Taken together, these experiments demonstrate that B508 treatment leads to an expansion of pyrimidine nucleotides, and selective imbalance in pyrimidine to purine nucleotide pools in cells which lack feedback control of *de novo* pyrimidine biosynthesis.

While the mitochondrial isoform of carbamoyl phosphate synthase (CPS1) is conventionally thought to initiate nitrogen disposal through the urea cycle, inherited urea cycle disorders caused by deficiency of distal components, including ornithine transcarbamylase (OTC), which produces citrulline from carbamoyl-phosphate and ornithine, result in orotic acidosis as CPS1 lacks allosteric regulation by UTP[25]. Similarly, we found CPS1 was upregulated without expression of OTC across sensitive cells (**Supplementary Figure 2d**) but we could not detect known disease-causing variants in any of the urea cycle enzymes (**Supplementary Table S3**). To determine whether flux through CPS1 was contributing to pyrimidine biosynthesis and nucleotide imbalance associated with B508 treatment, we followed the relative incorporation of $^{15}NH_4Cl$ into nitrogen containing metabolites across sensitive and resistant cell lines using our LC/MS based assay (**Supplementary Figure 3, Table S2**)[26]. In the presence of non-toxic levels (**Supplemental Figure 3e**), we found steady-state assimilation into a subset of amino acid, urea cycle and pyrimidine metabolites (**Supplementary Figure 3a,b,d**). While ammonia derived nitrogen was enriched in pyrimidine nucleotides across cell lines[27,28], we found sensitive cells had a four-fold increase in the relative fraction of ^{15}N-labeled carbamoyl-phosphate, which was depleted by CPS1 knockout (**Supplmentary Figure 3d**). Rather than assimilating ammonia into urea cycle metabolites downstream of carbamoyl-phosphate, we found an approximately equivalent increase in flux to pyrimidine nucleotides, independent of the rate of glutamine synthesis, which was sensitive to loss of CPS1 (**Supplemental Figure 3a-f**), suggesting that mitochondrial ammonia derived carbamoyl-phosphate was used for *de novo* pyrimidine biosynthesis. Consequently, ammonia increased the total pyrimidine nucleotide pool abundance in sensitive but not resistant cell types (**Supplemental Figure 3a**). As opposed to *de novo* pyrimidine biosynthesis, we found B508 treatment increased nitrogen assimilation into glutamate, and non-essential amino acids derived from glutamate transamination, leading to expansion of total abundance across resistant cell lines (**Supplemental Figure 3a-f**). Together, these experiments establish that sensitive cell types assimilate mitochondrial derived ammonia by *de novo* pyrimidine biosynthesis, as opposed to glutamate derived transamination in resistant cells.

To functionally validate whether increased pyrimidine biosynthesis drives B508 induced cell death, we measured viability after treatment with B508 in combination with DHODHi, in the presence of absence

of uridine[26]. Consistent with this hypothesis, co-treatment with DHODHi dose-dependently antagonized cell viability in the absence of uridine, and supplementation with uridine selectively rescued proliferation in response to DHODHi but not B508 (**Figure 2e, Supplementary Figure 3g**). As B508 treatment increased flux through CPS1, we also tested whether B508 could rescue viability in the presence of cytotoxic amounts of ammonia. In cells which maintained nucleotide homeostasis, treatment with B508 dose-dependently stimulated proliferation in the presence of ammonia (**Figure 2e**). As opposed to the proliferative defect caused by inhibitors of mitochondrial complex I or III, we could not observe depletion of glutathione after treatment with B508 at concentrations that inhibited complex IV and found B508 caused a dose-dependent degradation of TP53 in sensitive cell lines (**Supplementary Figure 4a**)[17,29,30]. Furthermore, addition of antioxidants did not rescue cell viability after treatment with B508 and we did not detect significant increases in PARP cleavage or upregulation of the pro-apoptotic, one-carbon, stress, and degradation pathways across sensitive cell types as opposed to DHODHi (**Supplementary Table 2, Supplementary Figure 3f**). These experiments demonstrate that increased pyrimidine biosynthesis leads to TP53 independent cell death in response to B508.

As transcription and replication fidelity requires balanced nucleotide pools[31], *de novo* pyrimidine biosynthesis is restricted to S-phase of the cell cycle. However, mitochondrial DNA (mtDNA) is continually replicated in proliferating cells[32]. Consequently, we found B508 selectively depleted poly-adenylated mtDNA encoded transcripts within three-hours across cell lines (P-value <1e-5, **Figure 2f, Supplemental Table S3**). The relative magnitude change in transcript abundance was proportional to the distance from the mtDNA origin and did not correlate with transcript length, suggesting B508 inhibits transcription but not mitochondrial ribosome translation. In contrast to transcription, we found B508 selectively reduced total mtDNA abundance across resistant cell lines after prolonged exposure, the magnitude of which was two-fold greater in comparison to sensitive cell lines (**Figure 2g**). Taken together these experiments demonstrate that like *de novo* pyrimidine biosynthesis, mitochondrial replication and biogenesis is maintained across sensitive in comparison to resistant cell lines, despite loss of nucleotide homeostasis.

As sustained mitochondrial replication and pyrimidine imbalance could challenge nuclear genome replication, we studied how pyrimidine expansion alters cell cycle progression and replication fidelity. Distinct from dNTP depletion through DHODH, or ribonucleotide reductase inhibition, we found that B508 treatment arrested asynchronously growing resistant cell lines in G1 at low concentration, or late S-phase at intermediary B508 concentrations with incomplete genome replication in comparison to G2/M nocodazole arrested cells (**Figure 2i,** upper panel, **Supplementary Figure 3d**). Like experiments following the incorporation of isotopically labeled uridine into pyrimidine nucleotides, we found S-phase arrested resistant cell lines-maintained uptake and incorporation of the thymidine analogue 5-bromo-2'-deoxyuridine (BrdU) into nuclear DNA in the presence of B508 (**Figure 2i**). This was distinct from sensitive cell types, which arrested in an ineffectual S-phase without uptake of BrdU, in line with continued *de novo* pyrimidine biosynthesis (**Figure 2i**). Despite incomplete replication, B508 dose-dependently increased the percentage of mitotic pH3 positive cells four-fold and increased the expression of mitotic kinases and spindle assembly proteins in sensitive but not resistant cell lines within 6-hours, which is significantly less than the basal time required for DNA replication (**Figure 3f, Supplementary Figure 4a,e**). We also found a significant subset of mitotic cells had condensed

chromatin abnormally aligned at the metaphase plate (Avg. 37% across five sensitive cell lines, **Supplementary Figure 4a, white arrows**).

Despite entry into mitosis, release into BrdU containing medium lacking compound demonstrated that sensitive cell types were capable of DNA synthesis (**Supplementary Figure 4f**), and we found EdU foci were localized at DAPI negative regions on mitotic chromosomes (**Supplementary Figure 4h**), indicative of replication stress[33]. To directly test whether B508 treatment inhibited replication, we labeled sensitive cells with IdU followed by treatment with B508 or aphidicolin in CldU containing medium and measured track length by DNA combing. Similar to aphidicolin, we found that B508 increased fork stalling and decreased track length (**Supplementary Figure 4g**). Moreover, B508 treatment increased the number of ɣ-H2AX foci across sensitive but not resistant cell types after 12–24-hour exposure to B508 (**Figure 2h**), and we found selective upregulation of DNA damage checkpoint and repair enzymes in sensitive cells (**Supplementary Figure 4a, Supplementary Table S3**). Contrastingly, G2/M checkpoint proteins were upregulated in response to B508 treatment across resistant cell lines (**Supplemental Figure 4a, Supplementary Table S3**). Taken together these experiments demonstrate that sustained nucleotide imbalance prevents complete replication, and induces mitotic catastrophe[34] in sensitive cells, whereas resistant cells arrest prior to mitosis and maintain DNA replication through pyrimidine salvage.

BMT-819/B508 Targets OXA1L and Repeat Expansion in the C-terminus Mediates Efficacy

To identify potential protein targets, we conducted chemical proteomic experiments using the photoreactive diazirine and alkyne substituents embedded in the parent probe[8,35]. We first compared the protein profiles enriched by BMT-819 to three inactive control probes, which represent distinct chemical space within the probe set and did not inhibit viability across the cell lines used for the initial toxicity screen (**Supplemental Figure 1b,** ≤1% change in viability across cell lines)[8]. In-situ photolabeling experiments using BMT-819 and inactive control BMT-182526 over a dose range of 0.04-10 µM, revealed selective labeling of ~37 kDa protein, beginning around the IC_{50} determined for cell viability, which was accompanied by a significant increase in additional background at 10 µM in H460 cells (**Supplementary Figure 2g,** red arrow). Mass-spectrometry based analysis of BMT-819 enriched proteins demonstrated a similar contrast, with a non-linear increase in the total reporter ion intensity in cells treated with >3 µM BMT-819 (**Supplemental Table S4**). Based on this dose range, we used 1 µM for follow-up studies and gel-based analysis revealed that the ~37 kDa band labeled by BMT-819 was unique in comparison to the inactive control probes (**Supplementary Figure 2g,** right), and was dose-dependently competed using the active competitor B508 (1-10 µM), but not inactive control 143-01 (**Supplementary Figure 2g**). Mass-spectrometry based-analysis of proteins selectively enriched by BMT-819 from H460 cells, revealed on average 59 of 2516 proteins identified across experimental conditions that were significantly enriched in comparison to three inactive probes or vehicle control across biological replicates (P Value < 0.0169, **Figure 2j**). Of these, 42 were known mitochondrial proteins[36], nine were direct components of the electron transport chain, including four integral complex V and three complex IV, in addition to the CIV insertase OXA1L, which was dose-dependently enriched starting at 100 nM (**Supplementary Table S4**, **Supplementary Figure 2h**)**.**

To complement the mass-spectrometry based identification of BMT-819/B508 associated targets, we used an unbiased genome-wide genetic screen to identify resistance conferring mutations or structural alterations in protein targets across cells with acquired resistance (**Figure 3, Supplemental Figure 5**)[37-40]. For the screen we selected three cell lines that were basally sensitive to BMT-819/B508, and previously

shown to acquire specific resistance to targeted small molecules toxins[37-40]. These include the mismatch repair deficient pseudo diploid cell line HCT116, in addition to karyotypically diverse cell lines H1792 and H460. From heterogeneous populations of barcoded versions of these cell lines (H460BC, H1792BC and HCT116BC), we produced resistance to BMT-819/B508 by continuous exposure to 150 nM of the active analogue B508 for a prolonged period of four-weeks, selected 10-20 clones from each parental cell line and reassessed the potency of B508 (light blue-individual resistant clones, dark blue-parental cells, **Figure 3a, Supplementary Figure 5a**). To reduce the likelihood that resistance was a result of increased compound excretion or metabolism we also assessed cross resistance to the anti-mitotic paclitaxel (light red-individual resistant clones, dark red-parental cells, **Figure 3a, Supplementary Figure 5a**)**.** While both HCT116 and H460 cells acquired specific resistance to B508, the relative shift in potency was greatest in H460, which became on average 17-fold less potent (Average IC_{50} = 0.44 μM, Parental IC_{50} = 0.035 μM, **Figure 3a**, **Supplemental Figure 5a**). In comparison, B508 efficacy was significantly decreased in H1792 cells without a significant shift in potency but was frequently accompanied by cross resistance to paclitaxel (**Supplemental Figure 5a**). Because B508 increases *de novo* pyrimidine biosynthesis, and cells that were basally sensitive to B508 were resistant to 5-FU (**Figure 1d**), we also evaluated the relative potency of 5-FU (gold) across cells with acquired resistance to BMT-819/B508. Although 5-FU potency was retained in a subset of B508 resistant clones, we found an overall collateral gain in sensitivity (IC_{50} = 0.0128 μM, decrease in viability >~90% of control) in comparison to parental cells (IC_{50} = 0.035 μM, decrease in viability <~50% of control) across all three cell lines, suggesting that the mechanism of resistance to B508 may impinge upon pyrimidine biosynthesis (**Figure 3a, Supplemental Figure 5a**).

To identify the mechanism conferring resistance to BMT-819/B508, we conducted whole genome sequencing across ten H460 clones that were selectively resistant to B508 and derived from unique progeny (**Supplemental Figure S5b**). Samples were sequenced to an average depth of ~36x and somatic variants were called against a panel of parental H460 clones (**Supplemental Table S4**). Consistent with B508 induced nucleotide pool imbalance, we found specific increase in mutational burden and copy number variation (CNV) at late-replicating regions, and a C>T mutational signature distinct from 8-oxoguanine induced oxidative DNA damage (**Supplemental Table 4, Supplementary Figure 4i, Supplementary Figure 5c**)[33,41,42]. To identify individual proteins mediating resistance, we analyzed genes with recurrent variation (**Supplementary Table S4**). Notably, the gene encoding OXA1L at chr14q11 was amplified across seven of the BMT-819/B508 resistant clones (**Figure 3f,g**, Average Log_2 Fold Change CN versus parent = 0.551), which we validated using fluorescence *in-situ* hybridization (**Figure 3f,** two versus three copies, n=30 metaphase spreads per clone, **Supplementary Table S4**). Importantly, OXA1L was the only protein selectively enriched by BMT-819 in chemical proteomic experiments (**Supplementary Table S4**), and in situ gel-based analysis demonstrated that labeling of the primary BMT-819 target (~37 kDa) was lost after CRISPR/Cas9 based OXA1L knockout (**Supplementary Figure 6a**). In clones that lack amplification of OXA1L, we identified a recurrent *de novo* missense mutation in its substrate MT-CO1[43] that changed a conserved threonine, which makes a direct interaction with the *heme* responsible for accepting electrons from cytochrome *c* to methionine (T31M), suggesting this variant would alter CIV function (**Figure 3j**, **Supplementary Figure 5i**).

In addition to its amplification, we found OXA1L was polymorphic in parental H460 cells, harboring a repeat expansion in the terminal exon (rs148216086), which RNA sequencing revealed was enriched across cell lines that were basally sensitive to BMT-819/B508 (**Figure 3e, Supplementary Table S3**). Importantly, this variant resulted in the extension of a polyserine repeat in the c-terminus of the OXA1L

protein (S419(AGC)$_5$, ENST00000604262), which we could selectively detect and quantify in enriched mitochondria via mass-spectrometry (**Supplementary Figure 5g,** KDNPPNIPSSSSSKPKS, M+H 1769.9028, 3 PSMs, XCorr = 5.0259), and protracted polyacrylamide electrophoresis (S419(AGC)$_4$-37 kDa and S419(AGC)$_5$-38 kDa, **Figure 4a, Supplementary Figure 5e**). In BMT-819/B508 resistant clones, amplification of OXA1L increased dosage of the wild type S419(AGC)$_4$ allele relative to parental cells (**Figure 3j, Supplementary Tables S4**), leading to an average two-fold increase in expression of the lower molecular weight isoform across clones with the additional copy (**Figure 3g,** 37 kDa). Despite OXA1L amplification, expression of its substrate MT-CO2, along with OxPhos complex III and DHODH, were decreased to similar levels as mitochondrial null H460 ρ˚ cells, independent of other mtDNA encoded OxPhos proteins, including MT-CO1 (**Figure 3g, Supplementary Figure 5f**). Moreover, proteomic analysis revealed that although all subunits of the mitochondrial ribosome were upregulated across heterozygous cell lines, the general abundance of mtDNA encoded OxPhos subunits were not (**Figure 3j**).

To further explore the association of OXA1L mutation and BMT-819/B508 resistance, we isolated an additional 30 clonal cell lines from parallel selections of H460 and HCT116 cells and sequenced the OXA1L cDNA from each. We identified 16 supplementary somatic missense mutations in the OXA1L gene in addition to the polymorphism, all of which cluster to the c-terminus (**Figure 3a**, **Supplementary Table S5**). These include L279V (1 clone), Q346H (2 clones), R358L (3 clones), R358S (3 clones), F365I (2 clones), R386Q (2 clones), and N387K (3 clones), which result in substitution of amino acids that make direct contact with the mitochondrial ribosome and/or nascent polypeptide substrates in aerobic organisms (**Figure 3c,d,k**)[44]. Notably, five of these variants were also identified in drug treated patient samples derived from refractory solid tumors of diverse origin[45], supporting their clinical relevance (**Supplementary Table S5**). To determine whether ectopic expression of OXA1L variants could confer resistance to BMT-819/B508, we stably expressed wild type and variant constructs in heterozygous parental H460 cells and assayed proliferation and viability (**Figure 3i**, **Supplementary Figure 6d, Supplementary Table S1**). In the presence of the parental allele, ectopic expression of the wild type OXA1L isoform, rescued proliferation (**Supplementary Figure 6d, Supplementary Table S1**) and decreased B508 potency 13-fold in comparison to cells expressing the S419(AGC)$_5$ variant alone or in combination with an additional c-terminal mutation, whereas sensitivity to paclitaxel was retained (**Figure 3i**). Contrastingly, expression of the S419(AGC)$_5$ constructs in basally resistant homozygous cells increased B508 efficacy (**Supplementary Figure 6e, Supplementary Table S1**). These experiments demonstrate that amplification of the wild type allele is sufficient to confer resistance in heterozygous cells, whereas expression of the S419(AGC)$_5$ variant in homozygous cells, increases sensitivity to BMT-819/B508.

Repeat Expansion Alters OXA1L-Substrate Affinity and Post-Transcriptionally Stabilizes DHODH-Dependent Respiration Independent of Complex I

To determine how OXA1L mutations impinge upon BMT-819/B508 efficacy, we conducted a set of functional assays and analyzed target engagement in H460 cells stably expressing ectopic wild type or variant OXA1L isoforms, in addition to H460 derived OXA1L knockout cells. We first confirmed that ectopic OXA1L constructs were successfully expressed and imported into mitochondria. Although both V5 epitope tagged wild type and S419(AGC)$_5$ isoforms displayed distinct mitochondrial localization, changing the amino acids downstream of the polyserine repeat (S424fSX13) or adding an additional mutation to S419(AGC)$_5$ resulted in increased cytosolic localization (**Supplementary Figure 6f,i**). Despite mitochondrial localization of S419(AGC)$_5$, *in situ* photolabeling experiments across ectopic OXA1L cell

lines demonstrated that the BMT-819 enriched two-fold more wild type OXA1L amid a decreased background labeling profile (**Supplementary Figure 6a,b**). Moreover, we found two-fold more OXA1L was enriched from homozygous H2009 in comparison to heterozygous H460 cells despite decreased total OXA1L expression across homozygous cells (**Supplementary Figure 6b**). These experiments suggest that BMT-819/B508 preferentially engages wild type OXA1L in the mitochondria.

As the OXA1L mutations were clustered to amino acids that contact the mitoribosome and/or nascent mitochondrial encoded polypeptides, we next analyzed OXA1L-substrate interactions by co-localization and co-immunoprecipitation (**Figure 4b**, **Supplementary Figure 6f,h,i**). While both wild type and S419$(AGC)_5$ variant isoforms were detected in the mitochondria, the wild type protein was significantly more colocalized with its substrate MT-CO2 in comparison to S419$(AGC)_5$ and co-immunoprecipitated two-fold more MT-CO2 in comparison to S419$(AGC)_5$ (**Figure 4b, Supplementary Figure 6h,i**). In opposition to basal co-immunoprecipitation and colocalization of MT-CO2, treatment of S419$(AGC)_5$ cell lines with B508 increased colocalization with and co-immunoprecipitation of MT-CO2, whereas B508 decreased co-immunoprecipitation and colocalization of MT-CO2 in wild type cells (**Figure 4b**). Consistently, B508 treatment dose-dependently depleted the lower molecular weight wild type OXA1L isoform in heterozygous H460 cells and increased the relative abundance of the higher molecular weight S419$(AGC)_5$ variant in the mitochondria (**Figure 4a**). These experiments demonstrate that the S419$(AGC)_5$ OXA1L mutation alters substrate affinity and is retained in the mitochondria in the presence of BMT-819/B508.

As OXA1L mutations altered affinity for its substrate MT-CO2, we measured the relative abundance of OxPhos complexes across ectopic cell lines in the presence or absence of BMT-819/B508. Despite increased affinity for MT-CO2, ectopic expression of the wild type OXA1L isoform decreased abundance of subunits of complex III, complex CIV, and DHODH, independent of complex I (**Figure 4d**). In contrast, ectopic expression of S419$(AGC)_5$ marginally increased expression of complex III, complex IV, and DHODH, relative to parental H460 cells, whereas OXA1L knockout depleted components of complex I, III and V (**Figure 4d**). Moreover, proteomic analysis of S419$(AGC)_5$ variant cells demonstrated that the general expression of mitochondrial proteins, including DHODH, complex III and complex IV, was retained in the presence of B508, and we found selective upregulation of the mitochondrial translation initiation factor MTIF3 and continued ^{13}C-Arginine/lysine incorporation into proteins from these complexes (**Figure 4a,e,f**). However, the mitochondrial ribosome inhibitor chroloramphenicol remained active irrespective of S419$(AGC)_5$ expression, suggesting that the OXA1L mutation is specifically associated with BMT-819/B508 activity. In comparison to S419$(AGC)_5$ variant cells, B508 treatment depleted mitochondrial protein abundance, inhibited mitochondrial translation, and decreased mitochondrial DNA content in cells expressing the wild type OXA1L isoform (**Figure 4a-d**). Taken together, these experiments suggest that the S419$(AGC)_5$ variant stabilizes the relative abundance of DHODH and complex IV, independent of complexes I, II and V, and remains functional in the presence of BMT-819/B508 in heterozygous cells.

To determine whether changes in OXA1L substrate expression had a functional impact on mitochondrial metabolism, we measured oxygen consumption and membrane potential across ectopic OXA1L cell lines. While expression of S419$(AGC)_5$ marginally increased basal OCR, we found that spare respiratory capacity was over 2-fold greater in comparison to wild type cells (**Supplementary Figure 6g**). Consistent with DHODH expression, the increased spare respiratory capacity in OXA1L S419$(AGC)_5$ cells was lost upon addition of DHODHi to the medium (**Supplemental Figure 6g**), suggesting the variant isoform

promotes DHODH dependent oxygen consumption. Furthermore, inhibition of DHODH significantly increased the number of H460 cells with biallelic OXA1L knockout after CRISPR/Cas9 mediated cleavage at exon 3 (**Supplementary Figure 6d**), and we found a collateral gain in sensitivity to 5-FU in wild type (IC_{50} = 0.0128 μM, decrease in viability >~90% of control), in comparison to S419$(AGC)_5$ variant cells (IC_{50} = 0.035 μM, decrease in viability <~50% of control). Although treatment with B508 dose-dependently inhibited OCR across cell lines, which was lost after OXA1L knockout, the relative decrease in cells expressing ectopic S419$(AGC)_5$ was significantly less than wild type or parental H460 cells, similar to the results obtained across heterozygous cancer cell lines (**Figure 1h-i**). To ascertain how sustained DHODH dependent respiration affected ΔΨm, we measured mitochondrial CMTMRos intensity after B508 treatment across ectopic OXA1L cell lines (**Figure 4g**). This analysis revealed that B508 selectively increased ΔΨm in S419$(AGC)_5$ variant cells, suggesting that complex V was impaired while DHODH dependent respiration was maintained (**Figure 4g**), consistent with the decrease in complex V expression after OXA1L knockout (**Figure 4d**). In contrast, B508 treatment decreased ΔΨm in cells expressing ectopic wild type OXA1L, similar to homozygous PC3 cells. Whereas expression of variant and wild type OXA1L isoforms altered response to B508, complex III inhibition decreased ΔΨm across both (**Figure 4g**). Taken together these experiments demonstrate that the S419$(AGC)_5$ OXA1L variant increases DHODH dependent respiration, which is maintained in the presence of BMT-819/B508, leading to mitochondrial hyperpolarization (**Figure 4i**).

1 Warburg, O., Posener, K. & Negelein, E. On the metabolism of carcinoma cells. *Biochemische Zeitschrift* **152**, 309-344 (1924).

2 Valle, S. *et al.* Exploiting oxidative phosphorylation to promote the stem and immunoevasive properties of pancreatic cancer stem cells. *Nat Commun* **11**, 5265, doi:10.1038/s41467-020-18954-z (2020).

3 Caro, P. *et al.* Metabolic signatures uncover distinct targets in molecular subsets of diffuse large B cell lymphoma. *Cancer Cell* **22**, 547-560, doi:10.1016/j.ccr.2012.08.014 (2012).

4 Nie, K. *et al.* COX6B2 drives metabolic reprogramming toward oxidative phosphorylation to promote metastasis in pancreatic ductal cancer cells. *Oncogenesis* **9**, 51, doi:10.1038/s41389-020-0231-2 (2020).

5 LeBleu, V. S. *et al.* PGC-1alpha mediates mitochondrial biogenesis and oxidative phosphorylation in cancer cells to promote metastasis. *Nat Cell Biol* **16**, 992-1003, 1001-1015, doi:10.1038/ncb3039 (2014).

6 Zhang, L. *et al.* Metabolic reprogramming toward oxidative phosphorylation identifies a therapeutic target for mantle cell lymphoma. *Sci Transl Med* **11**, doi:10.1126/scitranslmed.aau1167 (2019).

7 Son, J. *et al.* Glutamine supports pancreatic cancer growth through a KRAS-regulated metabolic pathway. *Nature* **496**, 101-105, doi:10.1038/nature12040 (2013).

8 Parker, C. G. *et al.* Ligand and Target Discovery by Fragment-Based Screening in Human Cells. *Cell* **168**, 527-541 e529, doi:10.1016/j.cell.2016.12.029 (2017).

9 Hafner, M., Niepel, M., Chung, M. & Sorger, P. K. Growth rate inhibition metrics correct for confounders in measuring sensitivity to cancer drugs. *Nat Methods* **13**, 521-527, doi:10.1038/nmeth.3853 (2016).

10 Ribic, C. M. *et al.* Tumor microsatellite-instability status as a predictor of benefit from fluorouracil-based adjuvant chemotherapy for colon cancer. *New Engl J Med* **349**, 247-257, doi:DOI 10.1056/NEJMoa022289 (2003).

11 Bracht, K., Nicholls, A. M., Liu, Y. & Bodmer, W. F. 5-Fluorouracil response in a large panel of colorectal cancer cell lines is associated with mismatch repair deficiency. *Brit J Cancer* **103**, 340-346, doi:10.1038/sj.bjc.6605780 (2010).

12 Mookerjee, S. A., Goncalves, R. L. S., Gerencser, A. A., Nicholls, D. G. & Brand, M. D. The contributions of respiration and glycolysis to extracellular acid production. *Biochim Biophys Acta* **1847**, 171-181, doi:10.1016/j.bbabio.2014.10.005 (2015).

13 Spinazzi, M., Casarin, A., Pertegato, V., Salviati, L. & Angelini, C. Assessment of mitochondrial respiratory chain enzymatic activities on tissues and cultured cells. *Nat Protoc* **7**, 1235-1246, doi:10.1038/nprot.2012.058 (2012).

14 Hao, W., Chang, C. P., Tsao, C. C. & Xu, J. Oligomycin-induced bioenergetic adaptation in cancer cells with heterogeneous bioenergetic organization. *J Biol Chem* **285**, 12647-12654, doi:10.1074/jbc.M109.084194 (2010).

15 Khacho, M. *et al.* Acidosis overrides oxygen deprivation to maintain mitochondrial function and cell survival. *Nat Commun* **5**, 3550, doi:10.1038/ncomms4550 (2014).

16 Hochachka, P. W. & Mommsen, T. P. Protons and anaerobiosis. *Science* **219**, 1391-1397, doi:10.1126/science.6298937 (1983).

17 Molina, J. R. *et al.* An inhibitor of oxidative phosphorylation exploits cancer vulnerability. *Nat Med* **24**, 1036-1046, doi:10.1038/s41591-018-0052-4 (2018).

18 Little, A. C. *et al.* High-content fluorescence imaging with the metabolic flux assay reveals insights into mitochondrial properties and functions. *Commun Biol* **3**, 271, doi:10.1038/s42003-020-0988-z (2020).

19 Romero, R. *et al.* Keap1 loss promotes Kras-driven lung cancer and results in dependence on glutaminolysis. *Nat Med* **23**, 1362-1368, doi:10.1038/nm.4407 (2017).

20 Pike Winer, L. S. & Wu, M. Rapid analysis of glycolytic and oxidative substrate flux of cancer cells in a microplate. *PLoS One* **9**, e109916, doi:10.1371/journal.pone.0109916 (2014).

21 Martinez-Reyes, I. *et al.* Mitochondrial ubiquinol oxidation is necessary for tumour growth. *Nature*, doi:10.1038/s41586-020-2475-6 (2020).

22 Salzman, N. P., Eagle, H. & Sebring, E. D. The utilization of glutamine, glutamic acid, and ammonia for the biosynthesis of nucleic acid bases in mammalian cell cultures. *J Biol Chem* **230**, 1001-1012 (1958).

23 Gerhart, J. C. & Pardee, A. B. The enzymology of control by feedback inhibition. *J Biol Chem* **237**, 891-896 (1962).

24 Watt, D. L., Buckland, R. J., Lujan, S. A., Kunkel, T. A. & Chabes, A. Genome-wide analysis of the specificity and mechanisms of replication infidelity driven by imbalanced dNTP pools. *Nucleic Acids Res* **44**, 1669-1680, doi:10.1093/nar/gkv1298 (2016).

25 Tischler, M. E., Pachence, J., Williamson, J. R. & La Noue, K. F. Mechanism of glutamate-aspartate translocation across the mitochondrial inner membrane. *Arch Biochem Biophys* **173**, 448-461, doi:10.1016/0003-9861(76)90282-4 (1976).

26 Zielinski, T., Zeitter, D., Muller, S. & Bartlett, R. R. Leflunomide, a reversible inhibitor of pyrimidine biosynthesis? *Inflamm Res* **44 Suppl 2**, S207-208, doi:10.1007/BF01778336 (1995).

27 Skaper, S. D., O'Brien, W. E. & Schafer, I. A. The influence of ammonia on purine and pyrimidine nucleotide biosynthesis in rat liver and brain in vitro. *Biochem J* **172**, 457-464, doi:10.1042/bj1720457 (1978).

28 Barton, P. A. & Hoogenraad, N. J. Effect of ammonium ion on pyrimidine synthesis de novo in isolated rat hepatocytes. *Eur J Biochem* **116**, 131-136, doi:10.1111/j.1432-1033.1981.tb05310.x (1981).

29 Goncalves, A. P. *et al.* Involvement of p53 in cell death following cell cycle arrest and mitotic catastrophe induced by rotenone. *Biochim Biophys Acta* **1813**, 492-499, doi:10.1016/j.bbamcr.2011.01.006 (2011).
30 Khutornenko, A. A. *et al.* Pyrimidine biosynthesis links mitochondrial respiration to the p53 pathway. *Proc Natl Acad Sci U S A* **107**, 12828-12833, doi:10.1073/pnas.0910885107 (2010).
31 Poli, J. *et al.* dNTP pools determine fork progression and origin usage under replication stress. *EMBO J* **31**, 883-894, doi:10.1038/emboj.2011.470 (2012).
32 Nishino, I., Spinazzola, A. & Hirano, M. Thymidine phosphorylase gene mutations in MNGIE, a human mitochondrial disorder. *Science* **283**, 689-692, doi:10.1126/science.283.5402.689 (1999).
33 Gaillard, H., Garcia-Muse, T. & Aguilera, A. Replication stress and cancer. *Nat Rev Cancer* **15**, 276-289, doi:10.1038/nrc3916 (2015).
34 Vitale, I., Galluzzi, L., Castedo, M. & Kroemer, G. Mitotic catastrophe: a mechanism for avoiding genomic instability. *Nat Rev Mol Cell Biol* **12**, 385-392, doi:10.1038/nrm3115 (2011).
35 Salisbury, C. M. & Cravatt, B. F. Optimization of activity-based probes for proteomic profiling of histone deacetylase complexes. *J Am Chem Soc* **130**, 2184-2194, doi:10.1021/ja074138u (2008).
36 Rath, S. *et al.* MitoCarta3.0: an updated mitochondrial proteome now with sub-organelle localization and pathway annotations. *Nucleic Acids Res* **49**, D1541-D1547, doi:10.1093/nar/gkaa1011 (2021).
37 Wacker, S. A., Houghtaling, B. R., Elemento, O. & Kapoor, T. M. Using transcriptome sequencing to identify mechanisms of drug action and resistance. *Nature Chemical Biology* **8**, 235-237, doi:10.1038/Nchembio.779 (2012).
38 Han, T. & Nijhawan, D. Exome Sequencing of Drug-Resistant Clones for Target Identification. *Methods Mol Biol* **1888**, 175-187, doi:10.1007/978-1-4939-8891-4_10 (2019).
39 Milhollen, M. *et al.* Treatment Emergent Mutations in NAE beta Confer Resistance to the NEDD8-Activating Enzyme Inhibitor MLN4924 in Pre-Clinical AML and DLBCL Models. *Blood* **118**, 615-615 (2011).
40 Han, T. *et al.* Anticancer sulfonamides target splicing by inducing RBM39 degradation via recruitment to DCAF15. *Science* **356**, doi:10.1126/science.aal3755 (2017).
41 Sima, J. & Gilbert, D. M. Complex correlations: replication timing and mutational landscapes during cancer and genome evolution. *Curr Opin Genet Dev* **25**, 93-100, doi:10.1016/j.gde.2013.11.022 (2014).
42 Alexandrov, L. B. *et al.* The repertoire of mutational signatures in human cancer. *Nature* **578**, 94-101, doi:10.1038/s41586-020-1943-3 (2020).
43 Thompson, K. *et al.* OXA1L mutations cause mitochondrial encephalopathy and a combined oxidative phosphorylation defect. *EMBO Mol Med* **10**, doi:10.15252/emmm.201809060 (2018).
44 Itoh, Y. *et al.* Mechanism of membrane-tethered mitochondrial protein synthesis. *Science* **371**, 846-849, doi:10.1126/science.abe0763 (2021).
45 Cancer Genome Atlas, N. Comprehensive molecular characterization of human colon and rectal cancer. *Nature* **487**, 330-337, doi:10.1038/nature11252 (2012).

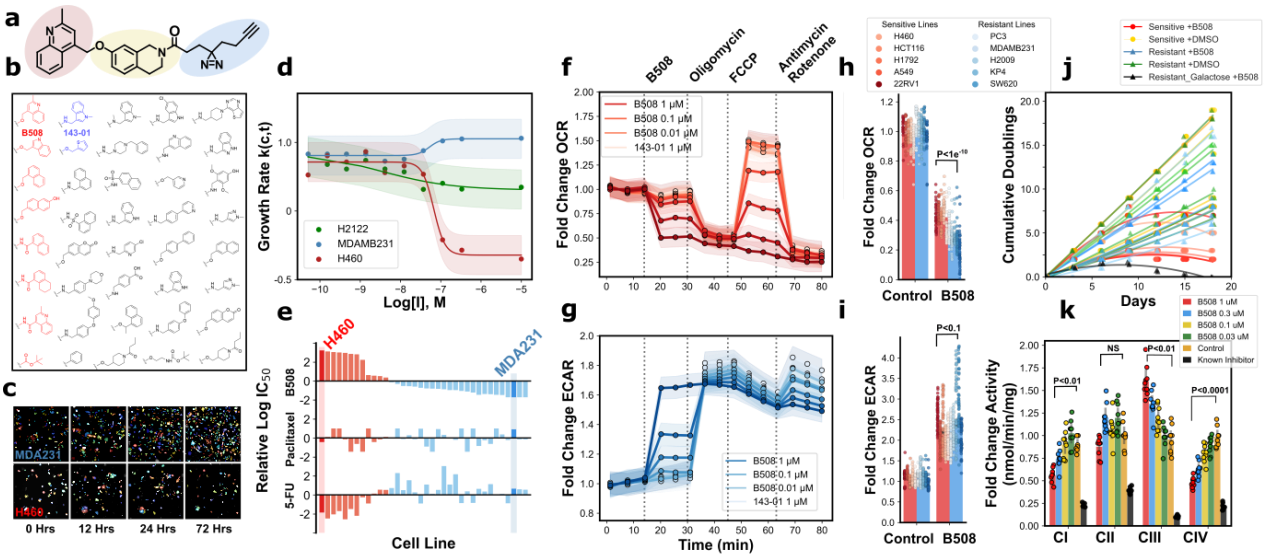

Figure 1: Small Molecules Targeting a Subset of Complex IV Dependent Oxygen Consumption Selectively Inhibit Proliferation

a, Structure of the photoreactive probe (BMT-819) identified from high-throughput screen (**Supplementary Figure 1**). **b**, Compound library generated to explore structure activity relationships (Bottom). Diazirine/alkyne moiety was replaced with butyramide at the tetrahydroisoquinoline ring (gold), and optimization of the 2-methylquinoline (blue) and ethyloxy linkage was explored. **c**, Representative images of resistant (MDA231) and sensitive (H460) GFP-labeled cell lines used for quantitation of growth rate inhibition calculated. **d**, Dose-response curves for growth rate-inhibition metrics calculated from cell count over 72-hour period in GFP expressing H460, H2122, and MDAMB231 cells (n=6 biological replicates). **e,** Bar graph of LogIC_{50} values calculated from 12-point dose-response curves after 72-hour treatment with B508 (red) in comparison to 5-Fluorouracil (white), and Paclitaxel (blue), across cell line panel. Each bar represents the mean of one individual cell line (*n*=3 biological replicates). Representative sensitive (H460) or resistant (MDAMB231) lines are outlined and labeled. **f,g,** Representative fold change in oxygen consumption (top) and glycolysis (bottom) in H460 cells assayed by Seahorse XF mito stress test with acute treatment of B508 or negative control 143-01 (10 minutes), over indicated dose range. Treatment with the known complex V inhibitor oligomycin (30 minutes), mitochondrial uncoupler FCCP (50 min), and combination of complex I and III inhibitors rotenone/antimycin A (65 min) following B508 or control treatment are shown (*n* = 3 biological replicates representative of ≥ 10 independent experiments). **h**, Fold change in oxygen consumption or **i**, glycolysis 10 minutes post treatment with B508 or control at concentration that elicits maximal change in OCR and ECAR (**Supplemental Figure 1c**) across five sensitive (red) or five resistant (blue) cell lines. Values show fold change from basal mitochondrial OCR or basal glycolytic ECAR across three technical replicates from *n*=6 biological replicates per cell line. Individual cell lines are separated on x axis and vary in color. Statistical significance was assessed using one-way ANOVA followed by Tukey's multiple comparisons test. **j,** Cumulative doublings over 20 days in five sensitive (red/gold) or resistant (blue/green) cell lines cultured in the presence of B508 (red or blue) at the IC50 determined in **e,** or DMSO control (gold or green) in complete medium exchanged daily. PC3 cells cultured in the presence of B508 in medium containing galactose as a substitute for glucose is shown in black. Each line represents the mean cumulative doublings per cell line (*n*=3 biological replicates, plotted individually

over the line. **k**, Fold-change in basal enzymatic activity of individual OxPhos components in mitochondria purified from H460 cells. Known inhibitors of each complex are shown as positive control (*n* = 8 biological replicates are plotted).

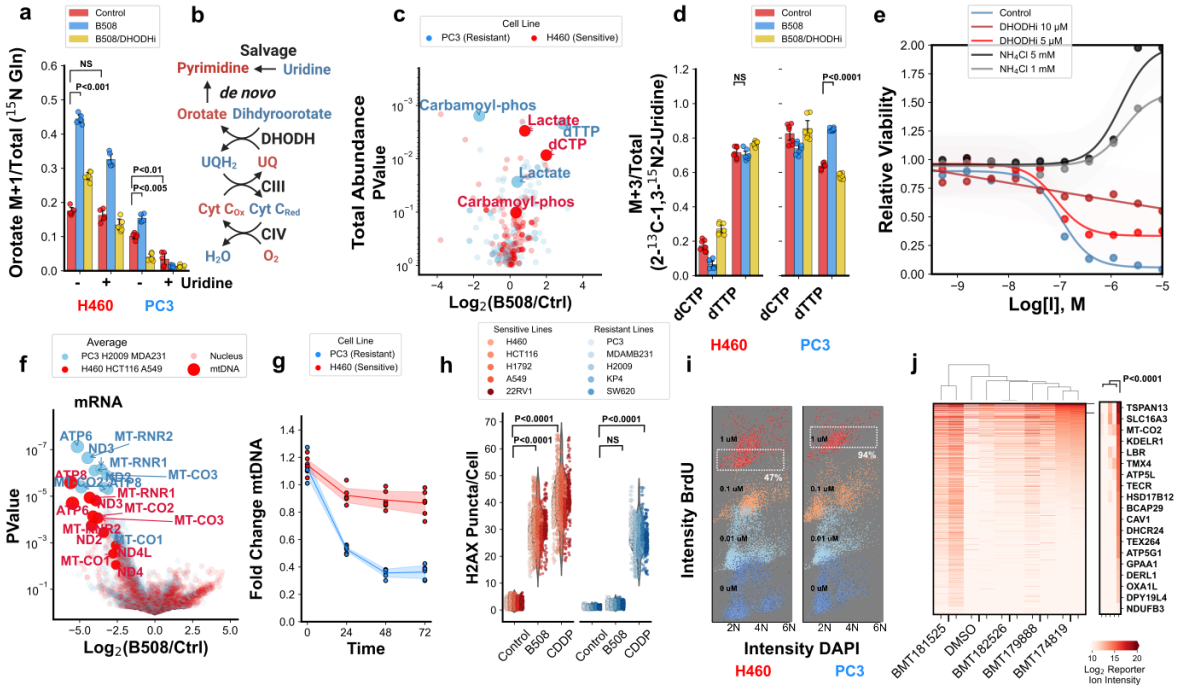

Figure 2: DHODH Dependent Oxygen Consumption is Maintained in the Presence of Inhibitor Leading to Imbalanced Nucleotide Pools and Mitotic Catastrophe

a, Relative percentage ^{15}N-Glutamine labeled M+1 Orotate in comparison to total metabolite pool in H460 or PC3 cells treated with B508 alone or in combination with DHODHi or control for 6 hours (*n*=5 biological replicates). Statistical significance was assessed using students t-test. **b,** Schematic depicting synthesis of dihydroorotate from glutamine or ammonia and coupling of DHODH with OxPhos complexes III, and IV. **c,** Volcano plot comparing B508 induced change in metabolite expression across either H460 (sensitive, red) or PC3 (resistant, blue) cells after 6-hour treatment. Deoxypyrimidine nucleotide triphosphates, and precursor carbamoyl-phosphate are labeled and significantly altered by B508 treatment. **d,** Relative fraction of M+3 isotopologue from 2-^{13}C-1,3-^{15}N2-Uridine in comparison to total metabolite abundance across H460 or PC3 cells treated with B508, B508 and DHODHi or control for 6 hours. Data are representative of *n*=3 biological replicates. Statistical significance was assessed using students t test. **e**, Viability after B508 treatment alone or in combination with DHODHi in the presence or absence of NH_4Cl (1 mm or 5 mM). **f**, Volcano plot showing change in transcript abundance in response to B508. Difference in mean basal transcript expression across three sensitive (red) and three resistant (blue) cell lines is shown. Mitochondrial encoded transcripts are labeled. **g,** Fold change in mtDNA abundance relative to nuclear Polɣ after treatment with B508 for indicated time. **h**, Relative ɣH2AX foci after treatment with B508 or cisplatin (CDDP) across five sensitive (red) and five resistant (blue) cell lines is shown. Number of foci was assessed by high content imaging and automated counting. Statistical significance was assessed using one-way ANOVA followed by Tukey's multiple

comparisons test. All experiments are the result of at least ≥3 independent experiments**. l,** Histogram showing BrdU verus DAPI intensity across cell lines treated with B508 at the indicated dose. Data are representative of *n*=6 biological replicates**. j,** Heat map visualization of TMT-based mass spectrometry analysis of proteins enriched by BMT-819 versus inactive controls. Structures are shown in **Supplementary Figure 1a**. Proteins that were significantly enriched (P Value <0.0001) by BMT-819 versus inactive controls across biological replicates are shown on the right.

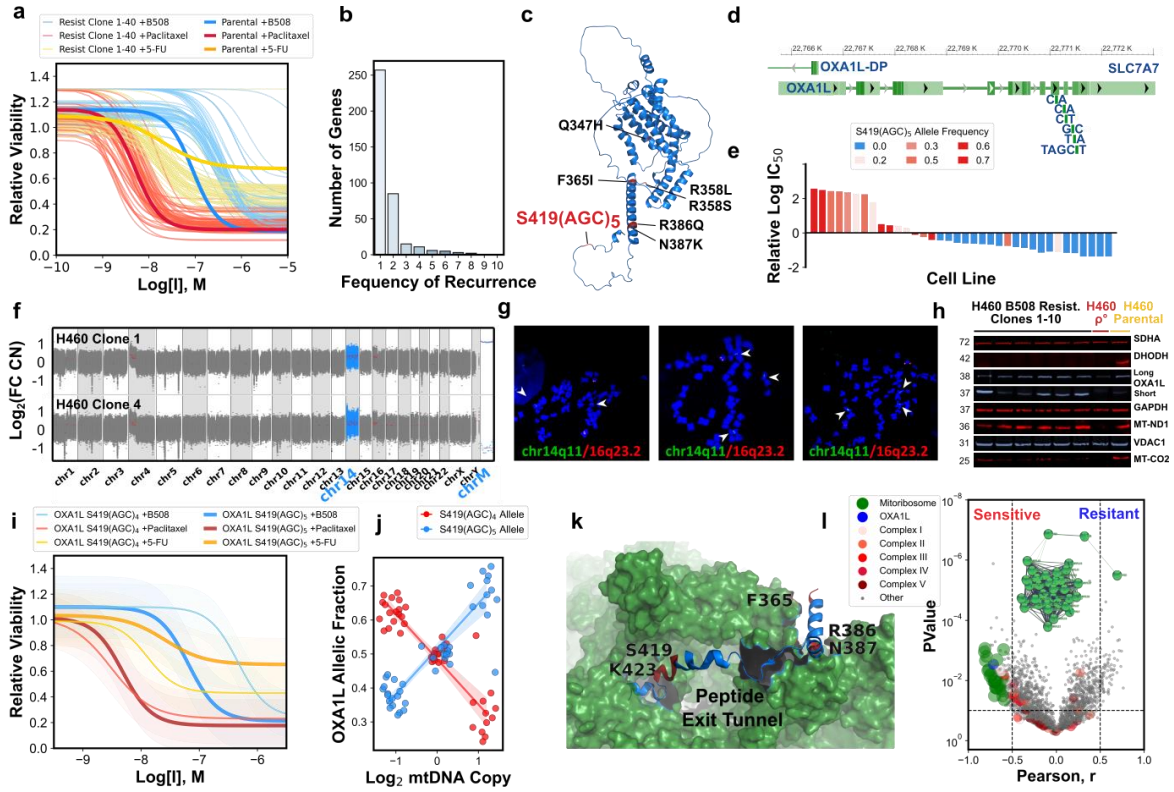

Figure 3: BMT-819/B508 Targets OXA1L and Repeat Expansion in the C-terminus Mediates Efficacy

a, Cell viability after 72-hour treatment with B508 (blue) or Paclitaxel (red) across individual clonal cell lines with acquired resistance to BMT-819/B508. Basal dose-response curves for each compound in Parental H460 cells are shown as bold lines. **b,** Number of genes with recurrent missense mutations across ten clonal cell lines with acquired resistance to BMT-819/B508. **c,** Missense mutations (red) in the OXA1L gene identified by whole genome sequencing across subset of H460 BMT-819/B508 resistant clones overlaid onto OXA1L protein structure (blue). **d**, Domain organization of OXA1L gene. BMT-819/B508 resistance mutations are clustered in the c-terminal tail, which is lost in anaerobic species (**Supplementary Figure 5b**). **e**, B508 potency and OXA1L S419(AGC)$_5$ allelic fraction across cell lines used for initial toxicity screen (**Figure 1e**). **f**, Copy number variants identified by whole genome sequencing across BMT-819/B508 H460 resistant clones. Selective and recurrent gain in wildtype chr14 and amplification or deletion of mtDNA is highlighted in blue (*n*=3 biological replicates per cell line). Red lines indicate significant CNV determined by statistical test of difference between the local insert size distributions of the reads around the candidate CNV in comparison to the global population. **g**, Representative metaphase spreads from H460 BMT-819/B508 Resistant clones 1 and 5 and parental H460 cells stained with chr14q11.2 probe (*n*=30 per 10 individual clones). Identified gain in normal

chr14q11 allele, ecDNA chr14q11 in clone 5 (White arrow). **h**, Protein abundance of representative components of OxPhos complexes across BMT-819/B508 resistant clones relative to parental H460 or H460 ρ˚ cells based on western blotting. **i,** Cell viability after 72-hour treatment with B508 (blue), 5-Fluoro uracil (gold), or Paclitaxel (red) in individual H460 cell lines with stable ectopic expression of OXA1L wild type or variant cell lines. Basal dose-response curve for each compound is shown as bold line. **j**, Correlation between OXA1L allelic fraction and relative mtDNA abundance across individual clonal cell lines with acquired resistance to BMT-819/B508 or parental H460 subclones. **k**, Cryo-electron micrograph of the c-terminal tail of OXA1L (gold) in complex with the mitochondrial ribosome peptide exit tunnel (green) (PDB 6ZM5). Amino acids affected by missense variants identified across H460 clones with acquired resistance are labeled and shown in blue. **l**, Volcano plot depicting correlation between protein expression, measured by TMT-based proteomics, and sensitivity to BMT-819/B508 across five sensitive and five resistant cell lines. Data represents mean of n=3 biological replicates per cell line. P-Value was calculated using student's t-test whereas negative or positive correlation between protein expression and B508 sensitivity is separated on the x-axis by Pearson, r. Components of individual OxPhos complexes and the mitoribosome are highlighted by color and size. Interactome of mitochondrial ribosome components found upregulated across sensitive cell lines is inset above the volcano plot, with edges representing experimental evidence from co-enrichment experiments.

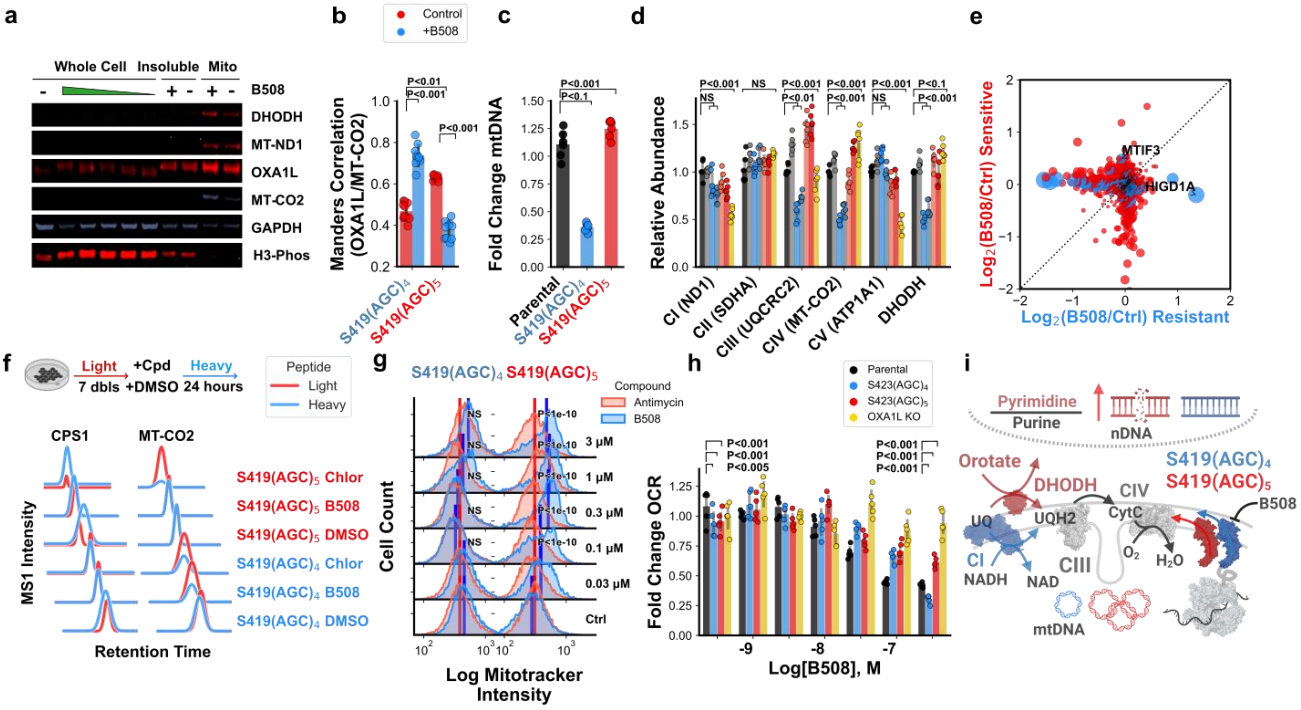

Figure 4: Repeat Expansion Alters OXA1L-Substrate Affinity and Post-Transcriptionally Stabilizes DHODH-Dependent Respiration Independent of Complex I

a, Subcellular fractionation, and analysis of OXA1L in addition to representative mitochondrial proteins encoded in the nucleus or mitochondria after treatment with indicated concentration of B508 for 3 hours by western blotting. Asterics indicate OXA1L isoforms. **b,** Unenriched proteomic analysis across three sensitive heterozygous OXA1L mutant (y-axis) and three resistant OXA1L wild type (x-axis) cell lines treated with B508 versus control (log_2 transformed). Proteins with known mitochondrial

localization are shown in blue. **c,** Biochemical analysis of mitochondrial localization in B508 treated H460 cells by western blotting. Representative mitochondrial (MT-CO2, MT-ND1) or nuclear encoded (OXA1L, DHODH) mitochondrial proteins and cytosolic (GAPDH) and nuclear (H3-phos) localized controls are shown. **d**, SILAC based proteomic analysis of cells pulsed with isotopically heavy medium containing B508, chloramphenicol (Chlor) or DMSO control for 24 hours. Extracted ion chromatograms for two representative peptides from nuclear (CPS1) and mitochondrial (MT-CO2) encoded proteins are shown. **e**, Relative oxygen consumption rate across parental or ectopic OXA1L variant cell lines in the presence of B508. **f**, Representative distribution of ΔΨm in ectopic OXA1L variant cell lines treated with B508 (blue) or Antimycin A (red) at indicated concentration by CMTMRos loading (log normalized). Welch's t-test was used to determine whether fluorescence intensity increased after drug treatment. Data are representative of *n*=3 independent biological replicates. **g**, Protein abundance of representative components of OxPhos complexes across ectopic OXA1L variant cell lines relative to confluent parental H460 cells based on western blotting. Data are expressed as mean ± SD and represent *n=3* biological replicates. **h**, Fold change in mtDNA abundance after ectopic expression of OXA1L variants across H460 cells. Data are expressed as mean ± SD and represent *n=4* biological replicates. **i**, Colocalization of OXA1L variant isoforms and complex IV component MT-CO2 in response to B508 (blue) or control (red). Quantification is shown in (**Figure 4h**). Data represent average values ± s.d taken from z-stack confocal images of 3 µM sections (**Supplemental Figure 6g**). **j,** Schematic of variant (red) or wild type (blue) OXA1L isoforms in relation to OxPhos complexes I, III and IV, DHODH and mitochondrial ribosome. Variant isoform stabilizes DHODH (light red) and respiration through DHODH and CIV is retained in the presence of BMT-819/B508, leading to pyrimidine imbalance, nuclear DNA damage and maintenance of mitochondrial biogenesis. Respiration through complex I (light blue) in wild type cells is coupled to complex IV leading to mitochondrial depletion (wild type).

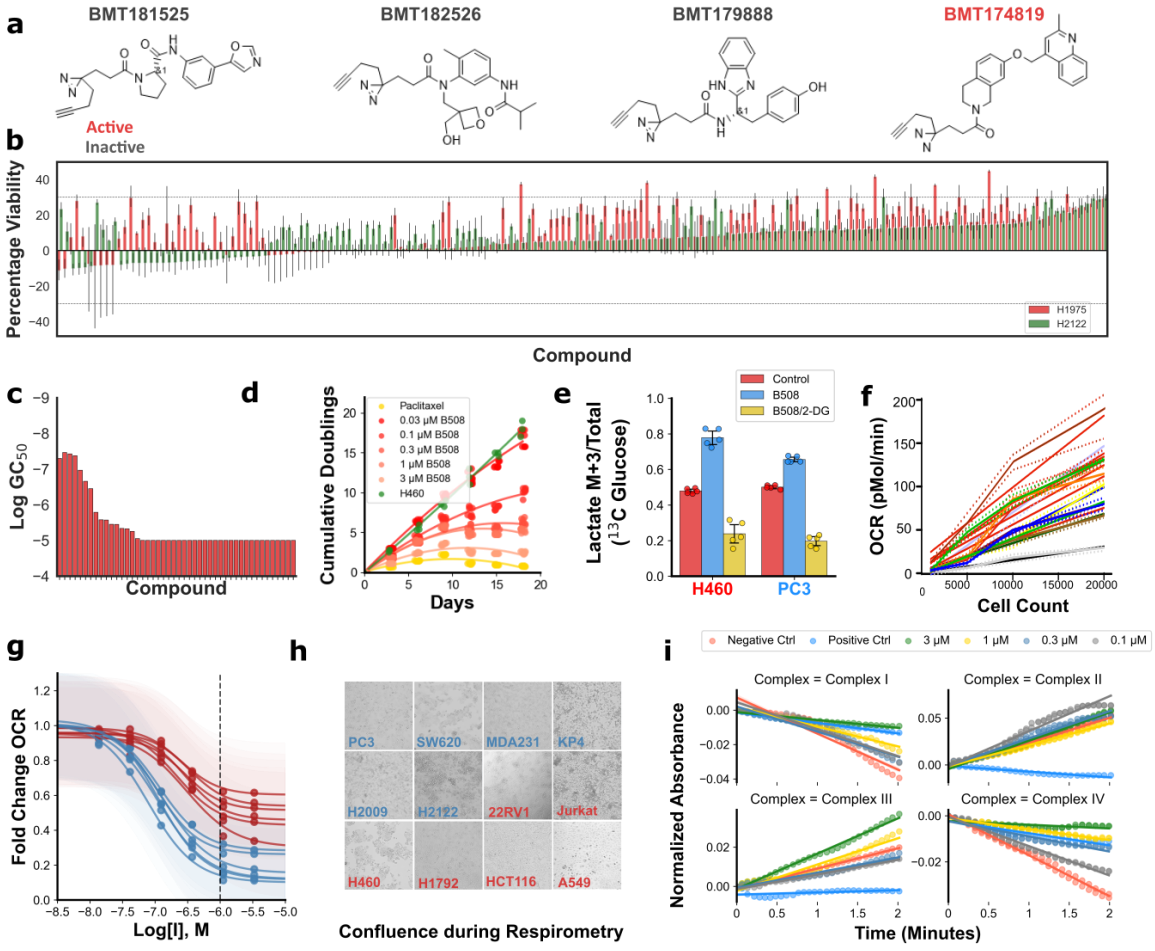

Supplemental Figure 1: Identification and Development of Cell Type Selective Small Molecules

a, Structures of representative compounds identified by viability screen in NSCLC cell lines. **b,** Bar graph of percent reduction in viability after 12-hour exposure of H1975 (red) or H2122 (blue) to 10 μM of diazirine/alkyne functionalized fragment library. Data represents mean (*n*=3 biological replicates) of compound treatment over aggregated vehicle controls, included for every eight compounds per plate. **c**, Counter screening of BMT-819 focused small molecule library by cell count and calculation of growth rate inhibition metrics over 72-hours. Bar graph shows LogGC_{50} for each compound (-5 shown for compounds that did not decrease growth rate by 50% at highest concentration 10^{-5} M). **d**, Cumulative population doublings of GFP expressing H460 cells exposed to varying concentrations of B508 over 15–20-day period with regular exchange of medium (*n*=3 biological replicates). **e**, Relative percentage U-^{13}C Glucose labeled M+3 lactate abundance relative to total pool in H460 or PC3 cells treated with B508 alone or in combination with 2-DG or control for 6 hours (*n*=5 biological replicates). **f**, Linear range of ECAR sensitivity across cell line panel evaluated by Seahorse SF assay. Lines represent mean ECAR for indicated number of cells with standard deviation illustrated by dashed line (*n*=3 biological replicates). **g**, B508 dose-response OCR measurements using optimized conditions shown in **f-h** (*n*=3 biological replicates). Saturating concentrations of B508 used for **Figure 1h,i** indicated by dashed line. **h**, Representative images of optimized Seahorse XF assay plating density across cell lines used for analysis. **i**, Basal enzymatic activity of individual OxPhos components in mitochondria purified from H460 cells.

Known inhibitors of each complex are shown as positive control. Data are representative of *n* = 8 biological replicates.

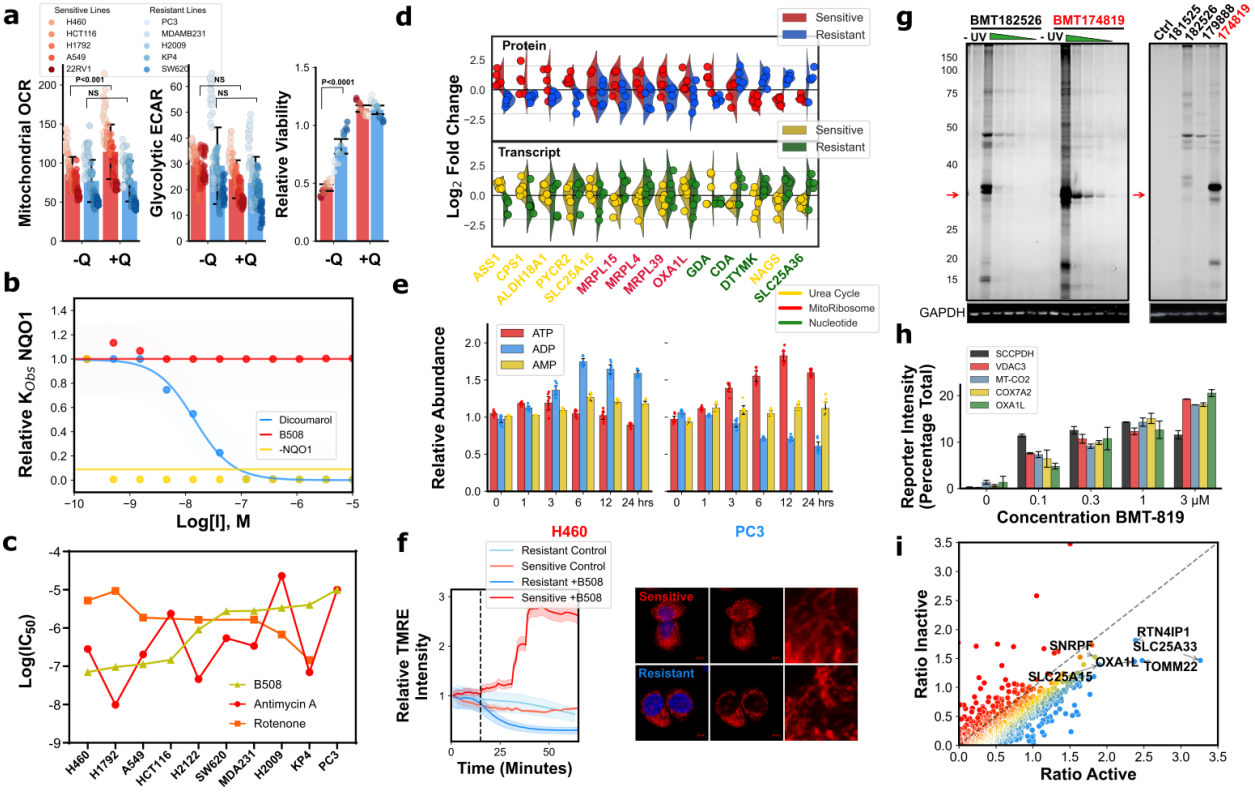

Supplemental Figure 2: Characterization of Mitochondrial Response to BMT-819/B508.

a, Basal metabolic phenotype across cell line panel in the presence or absence of glutamine. Mitochondrial OCR defined as the difference between basal OCR and residual OCR after treatment with Antimycin A and Rotenone. Glycolytic ECAR defined as magnitude decrease after treatment with 2-DG (*n*=6 biological replicates). **b**, Relative rate of cytochrome c reduction in NQO1 or mock transfected H460 cell lysates in the presence or absence of B508 or menadione at indicated concentrations. Data represents the mean and standard deviation of *n*=3 biological replicates **c,** Log IC_{50} of indicated OxPhos inhibitors across cell line panel determined by 12-point dose response celltiter glo assay after 72-hour exposure (*n*=3 biological replicates). Relative non-glycolytic ECAR induced by saturating concentrations of B508 in the presence or absence of glutamine across cell line panel. ΔECAR represents the mean absolute difference between B508 induced and 2-DG inhibited ECAR (*n*=6 biological replicates). **d,** violin plot depicting the most significant differences in protein or RNA expression associated with compound sensitivity measured by unenriched proteomics and RNA-seq across five sensitive and five resistant cell lines. Z-scored raw MS3 reporter ion intensity values or trimmed mean of m normalized read counts are plotted in with each point representing the mean (*n*=3 biological replicates per cell line). **e,** Relative change in adenine nucleotide abundance in H460 or PC3 cells treated with B508 in comparison vehicle control over indicated time (*n*=3 biological replicates). **f**, Relative TMRM fluorescence intensity with time in response to B508 or control in H460 (red) or PC3 (blue) cells. Data are representative of the mean

intensity over five z-planes normalized to time zero (*n*=2 biological replicates). **g**, Representative gel-based analysis of H460 cells labeled *in situ* with 0.04-10 µM BMT-819, BMT182526 (left), or three supplementary inactive control probes (right, structures shown in **Supplementary Figure 1a**) at 1 µM, followed by photo crosslinking and click reaction with rhodamine azide (*n*=4-6 biological replicates). Red arrows indicate dose-dependent and unique BMT-819-protein interactions. **h**, Mass spectrometry. **i**, **j**, **k**, Representative confocal images of PC3 or H460 cells transduced with RFP labeled pyruvate dehydrogenase leader peptide after 1-hour exposure to B508 at 500 nM. Representative kinetic assessment of individual OxPhos subunits assayed in H460 mitochondrial extracts. Absorbance was measured in the presence or absence of B508 with and without known inhibitors of each complex (*n* = 8 biological replicates).

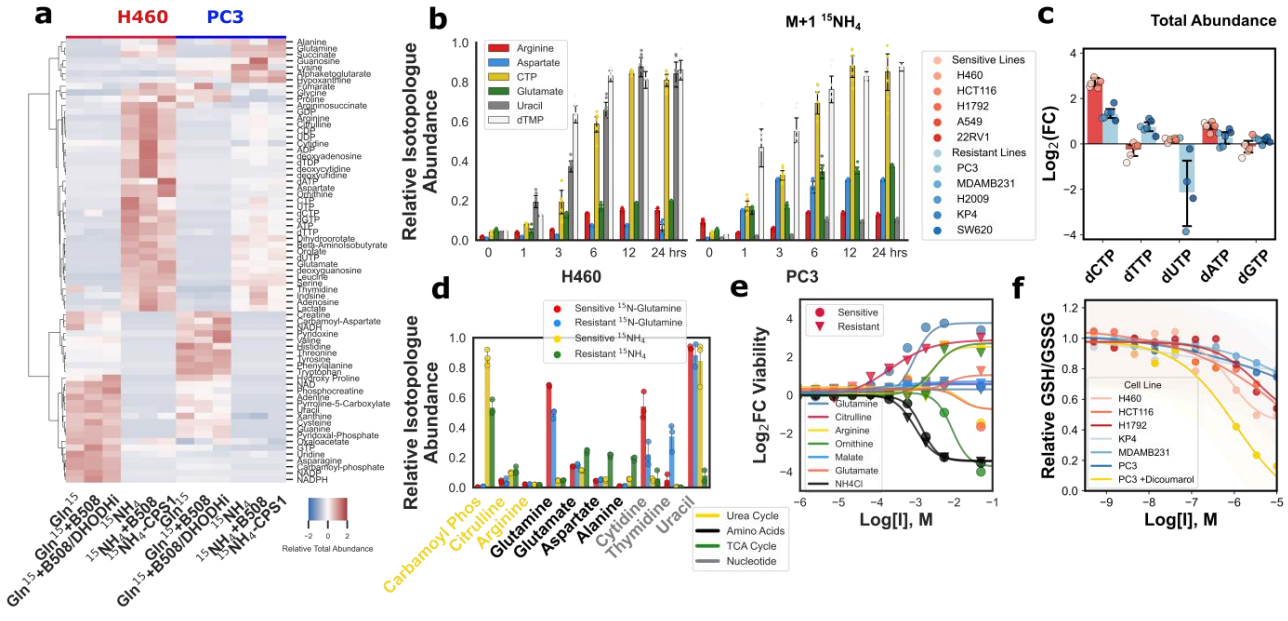

Supplemental Figure 3: BMT-819/B508 induces pyrimidine biosynthesis through CPS1

a, Heatmap showing relative change in total metabolite abundance in H460, PC3 or CPS1 knockout cells treated with B508, DHODHi or control for 6 hours. Values represent z-scored ion intensities normalized to protein concentration across *n*=3 biological replicates. **b**, Relative basal percentage M+1 isotopologue abundance in comparison to total metabolite pool from $^{15}NH_4Cl$ or ^{15}N-glutamine labeled H460 or PC3 cells over indicated time (*n*=3 biological replicates). Steady-state flux to pyrimidine nucleotides is achieved after 6-hour exposure in both cell lines. **c**, Change in deoxy nucleotide triphosphate levels after 6-hour treatment with B508 in comparison to DMSO control in three sensitive and three resistant cell lines during log-phase growth. Average for each cell line (*n*=3 biological replicates) is shown. **d**, Relative steady-state percentage M+1 isotopologue abundance from either $^{15}NH_4Cl$ or ^{15}N-amide glutamine labeled H460 or PC3 (*n*=6 biological replicates). **e**, Viability of sensitive or resistant cells in medium lacking glutamine, supplemented with indicated metabolite after 24-hours. **f**, Relative ratio of reduced/oxidized glutathione across cell types treated with variable B508 dose for 24 hours. **g**, **h**, **h**,

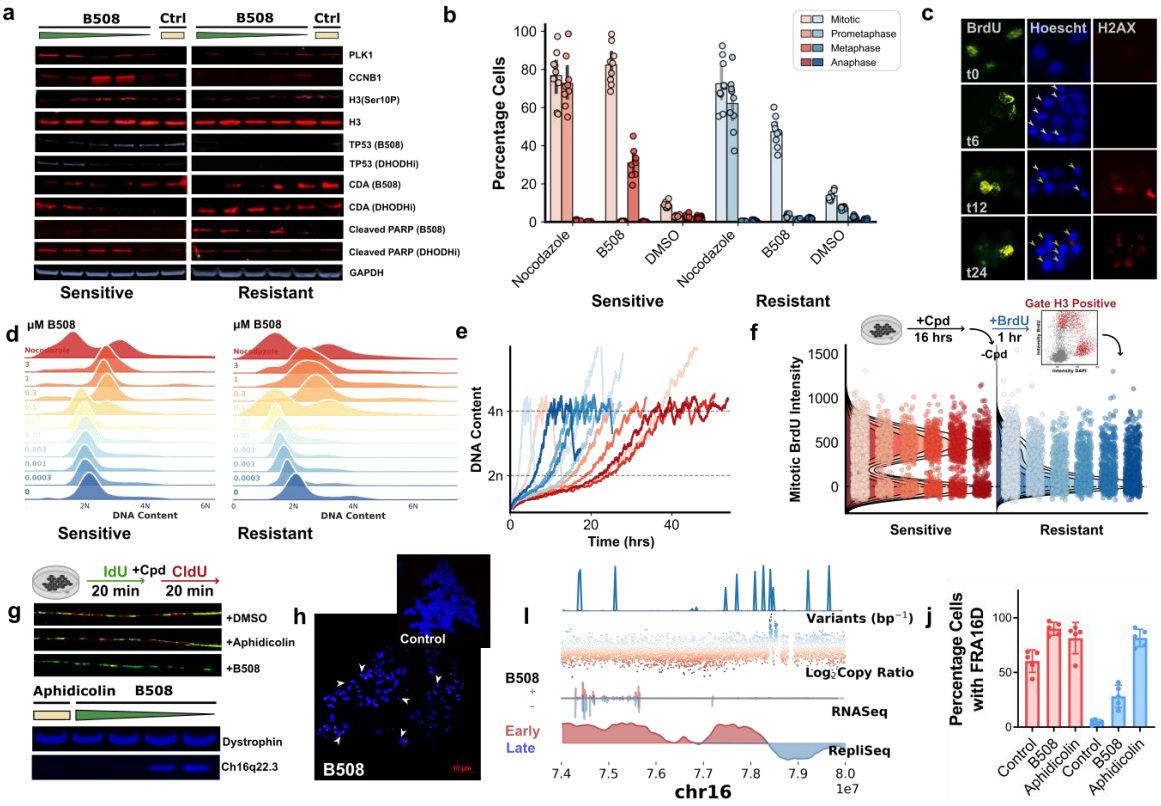

Supplemental Figure 4: Imbalanced pyrimidine pools results in replication stress and mitotic catastrophe

a, Expression of proteins associated with mitosis and apoptosis in sensitive (H460) or resistant (PC3) cells treated with B508 or control by western blotting. **b**, Quantification of cell cycle progression by confocal microscopy sensitive across sensitive (H460) or resistant (PC3) cells treated for 24 hours with B508, Nocodazole, or control (*n*=3 biological replicates). **c**, BrdU uptake, chromatin condensation (Hoescht) and γ-H2AX staining in sensitive (H460) cells treated with B508 for indicated time (*n*=3 biological replicates). **d**, Quantification of DNA content by DAPI across sensitive (H460) or resistant (PC3) cells treated for 24 hours with indicated dose of B508, Nocodazole, or control for 12 hours (*n*=3 biological replicates). **e**, Relative time to replicate nuclear DNA based on DAPI staining and proliferation rate across sensitive (blue) or resistant (red) cell lines. **f**, Quantification of BrdU uptake across sensitive (H460) or resistant (PC3) cells treated for 24 hours with B508 followed by release into BrdU containing medium lacking compound. **g**, Representative confocal images of individual DNA fibers taken from sensitive H460 cells pulsed with IdU, followed by CldU and indicated compound. **h**, Metaphase spreads from H460 cells treated with B508 or control for 12 hours. **i**, Variant density, copy number ratio, transcript abundance and replication timing at chr16q23 (FRA16D), quantified from whole genome or RNA sequencing data in one representative B508 resistant clone. **j**, Analysis of relative fragile site expression (FRA16D) by polymerase chain reaction across five sensitive (red) or five resistant (blue) cell lines treated for 24 hours with B508, aphidicolin, or control (*n*=3 biological replicates).

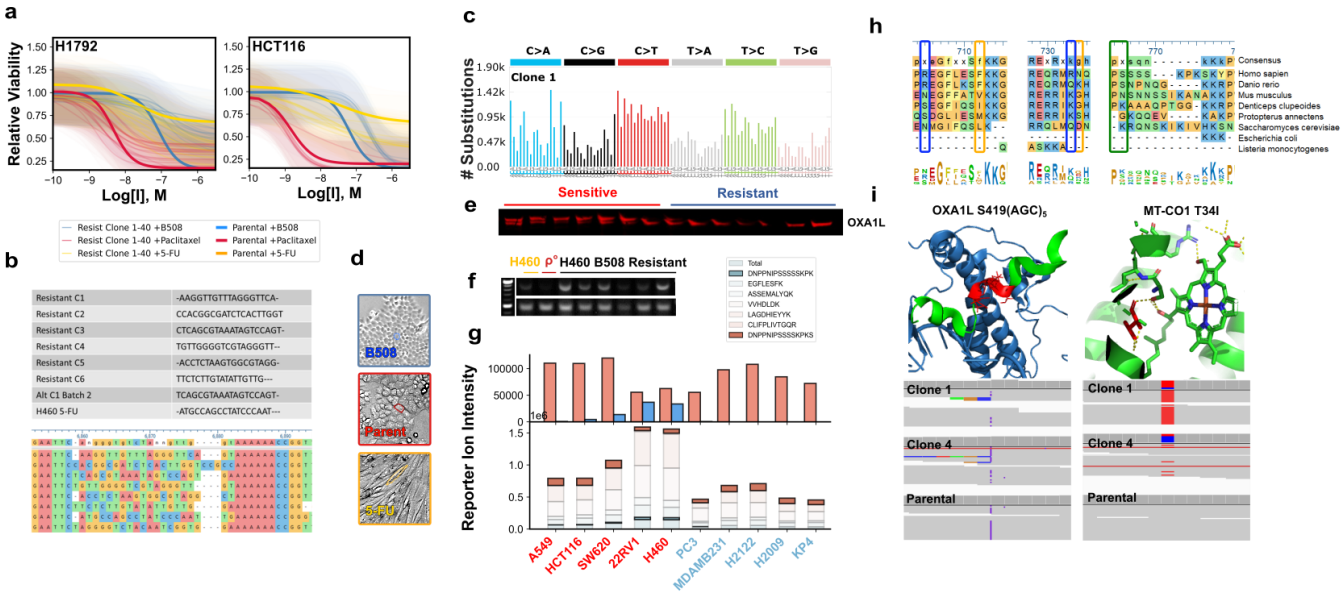

Supplemental Figure 5: Whole genome sequencing and characterization of BMT-819/B508 resistant clones

a, Cell viability after 72-hour treatment with B508 (blue) or Paclitaxel (red) in individual clonal cell lines with acquired resistance to BMT-819/B508. Basal dose-response curves for each compound is shown as bold line. **b**, Barcode sequences for individual clonal H460 cell lines used for whole genome sequencing. **c**, Characterization of mutational signature associated with somatic variants called from individual B508 resistant clone (Clone 1). Results representative of 10-clones. **d**, Brightfield images of representative B508 resistant clones (Top), parental H460 cells (Bottom). **e**, Characterization of OXA1L isoforms by protracted electrophoresis and western blotting across basally sensitive or resistant cell lines. Representative of *n=3* biological replicates. **f**, Mitochondrial DNA abundance across representative B508 resistant clones in comparison to H460 ρ° or parental cells. Mitochondrial tRNALeu (top), nuclear polymerase gamma (bottom). **g**, Relative reporter ion abundance of OXA1L peptides across subset of resistant (blue) or sensitive (gold) cell lines. Results are representative of *n=3* biological replicates. **h,** Conservation of OXA1L c-terminal tail harboring missense mutations identified in H460 resistant clones across aerobic and anaerobic species. **i**, Visualization of missense variants identified across B508 resistant clones (Top). OXA1L (left, 6ZM5), MT-ND5 (center, 5LDW), and MT-CO1 (right, 5Z62) are colored in green, with amino acids altered by mutation colored in red. Adjacent components included in the crystal structures are shown in blue. Aligned reads representative of variation in allele frequency across resistant clones are shown on bottom.

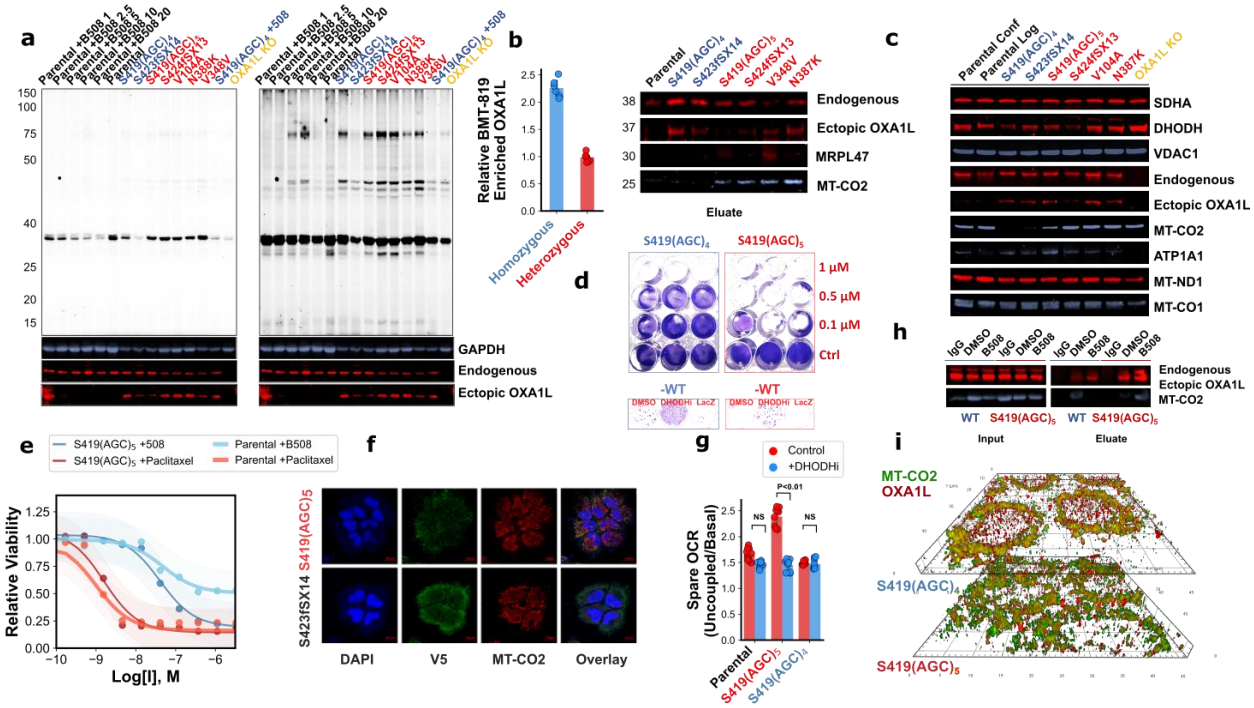

Supplemental Figure 6: Target engagement and functional studies across ectopic OXA1L variant cell lines

a, Representative gel-based analysis of parental H460, or OXA1L variant cells labeled *in situ* with 0.04-1 µM BMT-819, or BMT-819 and 10 µM active competitor B508, followed by photo crosslinking and click reaction with rhodamine azide (*n*=4-6 biological replicates). Red arrows indicate dose-dependent and unique BMT-819-protein interactions. **b**, Representative western-blot analysis of parental H460, or OXA1L variant cells labeled *in situ* with 1 µM BMT-819, followed by photo crosslinking, click reaction with biotin azide and enrichment on streptavidin beads. Eluates were probed with indicated primary antibodies (*n*=3 biological replicates). **c**, Protein abundance of representative components of OxPhos complexes across ectopic OXA1L variant cell lines relative to confluent parental (H460) cells based on western blotting (*n=3* biological replicates). **d**, Spare respiratory capacity across parental or ectopic OXA1L variant cell lines treated with vehicle or DHODH inhibitor. **e**, Western blots of proteins co-immunoprecipated with OXA1L antibodies or IgG control across variant or wildtype cell lines treated with and without B508. **f**, Crystal violet staining after 7-day exposure to B508 in OXA1L variant cells. **g**, Colocalization of OXA1L variant isoforms and complex IV component MT-CO2 in response to B508 (blue) or control (red). Quantification is shown in (**Figure 4h**). Data represent average values ± s.d taken from z-stack confocal images of 3 µM sections (**Supplemental Figure 6g**).